ADVANCED MATERIALS
www.advmat.de

Ultrapure Graphite from Solid Refining

Mingchao Ding, Zhibin Zhang, Wenya Wei, Heng Wu, Xue Chen, Jingwei Dong, Quanlin Guo, Mengze Zhao, Ziqi Zhou, Li Wang, Xiaozhi Xu, Ying Fu, Wei Yang, Muhong Wu, Quanzhan Yang, Feng Ding, Enge Wang, Pingheng Tan, Guangyu Zhang,* Kaihui Liu,* and Xuedong Bai**

Graphite has sparked extensive quantum physical discoveries and demonstrated numerous cutting-edge applications. However, existing graphite typically contains considerable impurities, and effective purification is still lacking. Here, a solid refining purification method is reported for obtaining ultrapure graphite. Through this design, impurities are filtered by the atomic lattice of a solid-state nickel (Ni). Suitable absorption, diffusion, and precipitation energy barriers are utilized in this method, allowing only carbon (C) atoms to effectively migrate through the Ni lattice to form high-quality graphite. The obtained ultrapure graphite shows the lowest elemental impurity density (<10 parts per million (ppm), which is one order of magnitude lower than that of the best available graphite), the highest structural purity (<0.2 parts per billion (ppb) of in-plane structural defect density and >99% Bernal stacking), and the highest doping purity (carrier doping density $<2.0 \times 10^{10}$ cm^{-2}). Such superior purity of graphite facilitates the all-integer visible Landau levels and the ultralow quantum transition magnetic field in the fabricated graphene device. This solid refinement technique should inspire the purification of various layered crystals, leading to the discovery of new phenomena and the development of advanced applications.

1. Introduction

High-purity materials have been pursued in materials science for centuries, ranging from salt production in the Agricultural Age to silicon (Si) purification in the Information Age. For most solid crystals, crystallization has shown its direct advancement in purification by precipitating pure crystals from a solution, melt, or vapor under controlled temperature or pressure gradient conditions.[1] Traditional salts and organic molecules with low melting points can easily crystallize by cooling or evaporating the solvent with the desired solute compounds near room temperature (e.g., sodium acetate from aqueous solution and menthol from peppermint oil). For metals and semiconductors with relatively high melting points (e.g., germanium (Ge): ≈938 °C, copper (Cu): ≈1084 °C, and Si: ≈1410 °C), the Czochralski[2] and Bridgman–Stockbarger[3,4] techniques are proven to be successful, involving the utilization of

M. Ding, J. Dong, L. Wang, W. Yang, G. Zhang, X. Bai
Beijing National Laboratory for Condensed Matter Physics
Institute of Physics
Chinese Academy of Sciences
Beijing 100190, China
E-mail: gyzhang@iphy.ac.cn; xdbai@iphy.ac.cn

M. Ding, J. Dong, W. Yang, G. Zhang, X. Bai
School of Physical Sciences
University of Chinese Academy of Sciences
Chinese Academy of Sciences
Beijing 100190, China

Z. Zhang, Q. Guo, M. Zhao, Z. Zhou, K. Liu
State Key Laboratory for Mesoscopic Physics
Frontiers Science Centre for Nano-optoelectronics
School of Physics
Peking University
Beijing 100871, China
E-mail: khliu@pku.edu.cn

W. Wei, X. Xu
Guangdong Basic Research Center of Excellence for Structure and Fundamental Interactions of Matter
Guangdong Provincial Key Laboratory of Quantum Engineering and Quantum Materials
Guangdong-Hong Kong Joint Laboratory of Quantum Matter
School of Physics
South China Normal University
Guangzhou 510006, China

H. Wu, X. Chen, P. Tan
State Key Laboratory of Superlattices and Microstructures
Institute of Semiconductors
Chinese Academy of Sciences
Beijing 100083, China
E-mail: phtan@semi.ac.cn

Y. Fu, M. Wu, X. Bai
Songshan Lake Materials Laboratory
Dongguan 523808, China

M. Wu, E. Wang, K. Liu
International Centre for Quantum Materials
Collaborative Innovation Centre of Quantum Matter
Peking University
Beijing 100871, China

The ORCID identification number(s) for the author(s) of this article can be found under https://doi.org/10.1002/adma.202500461

DOI: 10.1002/adma.202500461

small single-crystal seeds to slowly crystallize the melting sources into pure single crystals close to their melting points. For metal oxides with a higher melting point (e.g., sapphire: ≈2050 °C), crystallization can also be achieved in a tungsten crucible by the Kyropoulos method with a high process temperature.[5] However, for most van der Waals (vdW) layered materials with extremely high sublimation points (e.g., ≈3500 °C for graphite and ≈3000 °C for boron nitride), melting-based crystallization methods can hardly be utilized to fabricate them with ultrahigh purity. Currently, ultrapure vdW materials are eagerly desired due to their great potential for groundbreaking scientific discoveries[6–11] and cutting-edge applications.[12–15] However, their synthesis remains a significant challenge.

For typical vdW layered materials of graphite, due to their weak interlayer interactions, high density of silica, alumina, and iron compounds[16,17] accumulate between layers as extrinsic impurities, leading to the formation of intrinsic defects within layers. Till now, purified graphite still contains large amounts of impurities (e.g., ≈200 parts per million (ppm) for highly oriented pyrolytic graphite (HOPG), which is considered the best available graphite and is widely used in surface science research[18]). This characteristic greatly differs from the ultrahigh purities achieved in common metals using the melting-based purification method[19] (e.g., <10 ppm for Cu). Due to the inapplicability of melting-based crystallization for graphite purification, chemical leaching methods for removing the heteroatoms via acid reactions are generally employed. However, new chemical residue impurities are often inevitably introduced into graphite with the application of strong acids. To eliminate these residues, high-temperature treatment is subsequently applied, while also leaving the high melting point impurities and additional lattice defects (stacking faults and grain misorientations) under such extreme environments. An effective method for obtaining ultrapure graphite by simultaneously eliminating heteroatoms and preserving lattice configurations is in great demand but has yet to be discovered.

Here, we develop a nontrivial solid refining method for obtaining ultrapure graphite by repeatedly dissolving, diffusing, and precipitating carbon (C) atoms within single-crystal nickel (Ni) foil,[20] which enables the purification of graphite at a temperature (1200–1300 °C) of only about one-third of its sublimation point. Due to the high selectivity of the Ni lattice, all other heteroatoms are blocked, and only C atoms can effectively migrate through Ni to form high-quality graphite. Avoiding traditional aggressive treatment, the obtained ultrapure graphite not only exhibits the highest elemental, structural, and doping purities but also maintains large-scale single crystallinity under this low-temperature refining process (Table S1, Supporting Information). Furthermore, high-quality monolayer graphene could be exfoliated from ultrapure graphite and was utilized to fabricate quantum Hall devices, enabling the explicit observation of extraordinary quantum transport phenomena.

Q. Yang, E. Wang
School of Physics, Liaoning University
Shenyang 110036, China
F. Ding
Shenzhen Institute of Advanced Technology
Shenzhen 518055, China
E. Wang
Tsientang Institute for Advanced Study
Hangzhou 311225, China

2. Results

In the solid refining process to obtain ultrapure graphite, we designed a filtration-like mechanism by utilizing the atomic lattice of Ni as the filter, where low-purity carbon sources were placed on one side of the Ni foil to be filtered (**Figure 1a**). The atoms in the carbon sources could diffuse through Ni to the opposite surface by overcoming the barriers of absorption (I to III), diffusion (IV to VI), and precipitation (VII to IX) in the Ni lattice (Figure 1b). This process can be performed to produce a highly purified graphite sample only when (i) heteroatoms display high values in any of the absorption, diffusion, and precipitation barriers, and (ii) C atoms exhibit low values in all of these three energy barriers simultaneously.

By comparing the energy profiles of common elements in carbon sources via theoretical density functional theory (DFT) calculations, we find that most of the elements exhibit high energies (>2 eV atom^{-1}) in bulk Ni, suggesting a low probability of diffusion through the Ni lattice (Figure 1c). Notably, there are three elements exhibit low energy levels (<2 eV atom^{-1}) in Ni bulk, i.e., Si, boron (B), and C. Detailed energy barrier calculations demonstrate that i) Si atoms exhibit a high energy barrier of 3.32 eV atom^{-1} from I to II (Figure 1d, top panel), indicating their low absorption probability from Ni surface into bulk; and ii) B atoms exhibit a negative formation energy of −0.47 eV atom^{-1} in IV with the tendency to form a Ni-B alloy[21] (Figure 1d, bottom panel), showing their great difficulty in precipitation from Ni bulk to surface. In contrast, C atoms have low absorption barriers (0.42 eV atom^{-1}) from Ni surface into bulk and positive formation energies (0.37 eV atom^{-1}) in bulk Ni (Figure 1d, bottom panel). Besides, C atoms also possess moderate diffusion energy barriers (1.68 eV atom^{-1}) through the Ni lattice and precipitation barrier (1.04 eV atom^{-1}) from the Ni bulk to the opposite Ni surface, facilitating the purification of graphite at the growth temperature. These results confirm that the atomic lattice of Ni is an optimal platform for the solid refining process to selectively pass the C atoms and block the heteroatoms, finally producing the ultrapure graphite.

For the first solid refining cycle, the single-crystal Ni foil was pressed onto graphite paper and heated to 1200–1300 °C (Figure 1e, other low-purity carbon sources can also be used, shown in Figure S1, Supporting Information). A few impurity atoms could migrate through the Ni lattice due to their excessive quantities in graphite paper. Then, another single-crystal Ni was utilized to prevent the diffusion of these remaining impurities. This second refining cycle removed nearly all the residue impurities, significantly decreasing the number of extrinsic impurities, as characterized by inductively coupled plasma–mass spectrometry (ICP–MS) (Figure 1f). By repeating the solid refining process once more, ultrapure graphite was obtained with the lowest extrinsic impurity density (<10 ppm, approaching the detection limit of the mass spectrometry we used) among all kinds of high-quality graphite (Figure S2, Supporting Information). This impurity density was one order of magnitude lower than that of the current purest graphite, namely, HOPG.

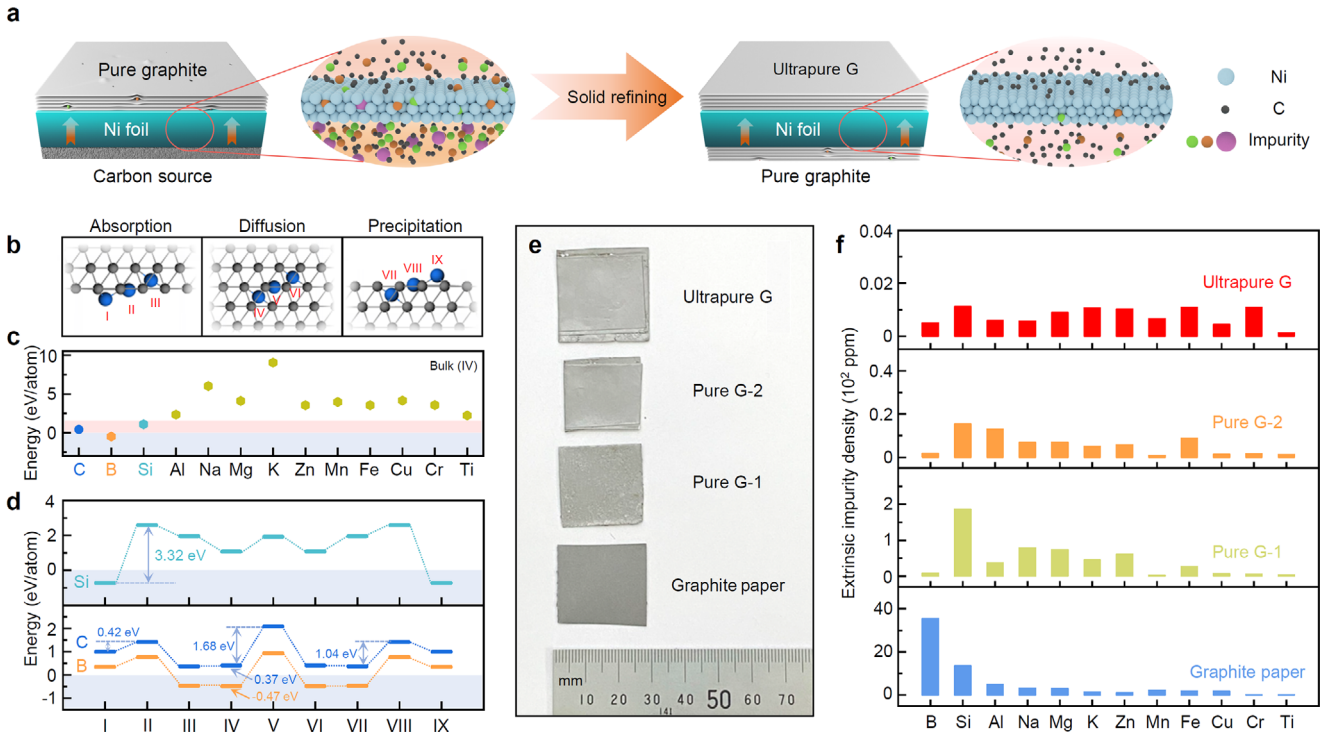

Figure 1. Solid refining purification and elemental purity characterization. a) The diagram of the solid refining process to obtain ultrapure graphite (ultrapure G). b) The atom transport process through the Ni lattice. In the absorption process (left panel), the atom transports from the Ni bottom surface (I-II) into Ni bulk (III). In the diffusion process (middle panel), the atom transports from one Ni lattice cell (IV), through the Ni cell boundary(V), and into another Ni cell (VI). In the precipitation process (right panel), the atom transports from Ni bulk (VII), through the Ni top surface (VIII), and precipitates out on the top surface (IX). c) The energy of different atoms dissolved into Ni bulk. d) Energy profiles of Si, C, and B atoms diffusing through the Ni lattice. e) Photograph of graphite paper and samples after one (pure G-1), two (pure G-2), and three (ultrapure G) refining cycles. f) The extrinsic impurity density measured by ICP-MS of different samples in (e).

Besides, the in-plane structural defects, including point and line defects, usually exist in graphite due to heteroatom doping and chaotic domain alignments. Through the solid refining process, the elemental purity in ultrapure graphite was sufficiently improved and thus could, in principle, lead to a distinct purification in the in-plane structural defect density. As these atomic defects are thermodynamically unstable, hydrogen (H_2) plasma was introduced to etch these defect sites into hexagonal pits[22] (Figure S3a, Supporting Information). After hours of etching, these pits or ravines will be large enough and could be readily visualized through atomic force microscopy (AFM) measurements (Figure S3b–d, Supporting Information). An obvious decrease in intrinsic point defects was observed in purified graphite during the refining process (**Figure** 2a_1–a_3). The obtained ultrapure graphite exhibited an ultra-flat surface without visible pits or steps (Figure 2a_3), demonstrating that its intrinsic defect density was extremely low (<0.01 μm^{-2}, Figure S4a, Supporting Information, corresponding to <0.2 parts per billion (ppb) in bulk graphite), approaching the AFM detection limit. In contrast, large amounts of pits and ravines were observed on the surfaces of the kish graphite, HOPG, and natural graphite under the same etching conditions (Figure 2b_1-b_3), indicating that their intrinsic defect densities were about two orders of magnitude higher than those of ultrapure graphite (Figure 2c, the defect densities was calculated based on a 5 × 5 μm^2 AFM measurement).

In the further larger-scale AFM experiments, we observed that all the hexagonal pits of ultrapure graphite under H_2 etching were parallel to each other (Figure S4b, Supporting Information), distinctly contrasting with the relatively poor alignments (limited in tens of micrometers) in HOPG (Figure S4c, Supporting Information). Such parallel configurations demonstrated the large-scale single crystallinity of ultrapure graphite, which was further confirmed by the centimeter-scale uniform color in electron back-scattered diffraction (EBSD) experiments (Figure 2d_1-d_4; other graphite samples typically display domains of ≈ 100 μm).

In addition to the in-plane lattice structure, the out-of-plane lattice stacking configuration of our ultrapure graphite was confirmed to be Bernal (2H) stacking (with an interlayer spacing of 0.335 nm) through atomically resolved cross-sectional scanning transmission electron microscopy (STEM) measurements at the nanoscale (Figure 2e). The identical interlayer distance was also confirmed by high-resolution X-ray diffraction (HR-XRD) measurements (Figure S5, Supporting Information). Owing to the in-plane hexagonal lattice structure and out-of-plane weak vdW interlayer couplings of graphite, another phase, the rhombohedral (3R) stacking order, also frequently emerges (**Figure** 3a). Consequently, stacking faults would arise when the sequential order of graphene layers within the crystal lattice is disrupted. For the comprehensive macroscale detection of the stacking sequences, we conducted low-frequency Raman spectroscopy experiments (Figure 3b,c). The shear mode (E_{2g}) peak corresponds to the

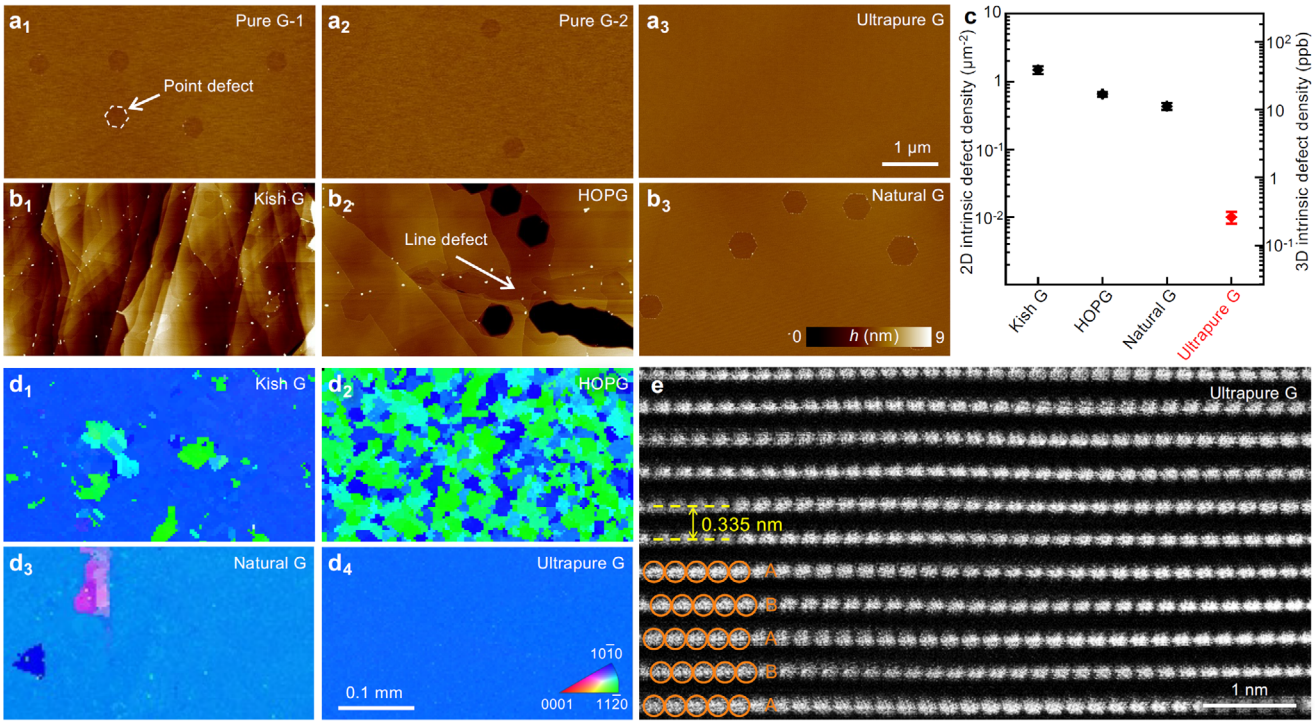

Figure 2. In-plane structural purity characterization. a_1-a_3), The AFM images of graphite after different refining cycles under H_2 plasma etching. b_1–b_3), The AFM images of commercial graphite after H_2 plasma etching (kish graphite (b_1), HOPG (b_2), and natural graphite (b_3)). Typical point defect vacancy and line defect are marked in (a_1) and (b_2), respectively. c), The calculated intrinsic defect density of different graphite samples. d_1–d_4), The EBSD maps along the X direction of the inverse pole figure of kish graphite (d_1), HOPG (d_2), natural graphite (d_3), and ultrapure graphite (d_4). e), The cross-sectional atomically resolved STEM image of ultrapure graphite.

coupled oscillations in the interlayer phonon mode, and both the 3R stacking configuration and stacking faults will weaken the E_{2g} peak intensity.[23,24] In our Raman experiments, ultrapure graphite demonstrated the highest E_{2g} intensity among all the graphite samples (Figure 3d and see Experimental Section for more details), suggesting its purest 2H stacking phase and the fewest stacking faults.

The out-of-plane structural purity could be quantitatively confirmed by in-plane electrical measurements as well, where the measured resistivity could be regarded as a combination of the parallel resistances of domains with different stacking sequences (R_{2H} for 2H stacking and R_{3R} for 3R stacking) and the interfacial residual resistance between domains (R_{ITF}) (Figure 3e). The room-temperature resistivity of ultrapure graphite was found to be the lowest among all the samples (Figure 3f; Figures S6 and S7a, Supporting Information), preliminarily demonstrating its ultrahigh purity with less electron scattering. Temperature-dependent resistivity measurements were subsequently conducted (Figure 3g). The resistivities of ultrapure graphite and natural graphite presented a metallic behavior with a decreasing tendency when the temperature was reduced, while those of kish graphite and HOPG exhibited a combination of metallic and semiconducting behaviors with saturated resistivities at low temperatures. The normalized temperature-dependent resistivities (Figure S7b, Supporting Information) with the R_{2H}, R_{3R}, and R_{ITF} were analyzed (Table S2, Supporting Information, see Experimental Section for more details). We found that both the normalized interfacial residual resistance (R_0) and the 3R phase weight ratio of the ultrapure graphite reached the minimum (Figure 3h). This reveals the purest 2H phase (η_{2H} >99%, see Experimental Section for more details) and the fewest stacking faults in our ultrapure graphite.

Carrier doping is considered another critical factor that needs to be carefully assessed for an ultrapure material because residue doping would severely affect electronic properties by chaotic scattering and mobility reduction.[25] We first evaluated the doping purity of our ultrapure graphite by performing Raman spectroscopy on its exfoliated monolayer encapsulated with hexagonal boron nitride (hBN) flakes. A small full width at half maximum (FWHM) (≈15.7 cm^{-1}) of the Raman 2D peak (**Figure 4a**) was obtained, lower than the typical value (16–18 cm^{-1}) of the exfoliated graphene samples reported in the literature.[26–28] The intensity ratio between the 2D peak and the G peak (I_{2D}/I_G) also reached an ultrahigh value of 12 compared to previous results (I_{2D}/I_G is typically ≈ 6–10).[26–28] This smallest FWHM and highest I_{2D}/I_G are attributed to the uniform strain distribution and the ultralow carrier doping of our graphene samples.[27] To clarify the doping level, we further fabricated a standard Hall device using monolayer graphene exfoliated from the ultrapure graphite sample (Figure 4b). The low temperature (1.7 K) transfer curves show that the neutral point doping density of ultrapure graphite is the closest to zero (Figure 4c), with the initial carrier doping density calculated to be smaller than 2.0×10^{10} cm^{-2}. This value is better than those in typical works of graphene transport measurements.[29,30]

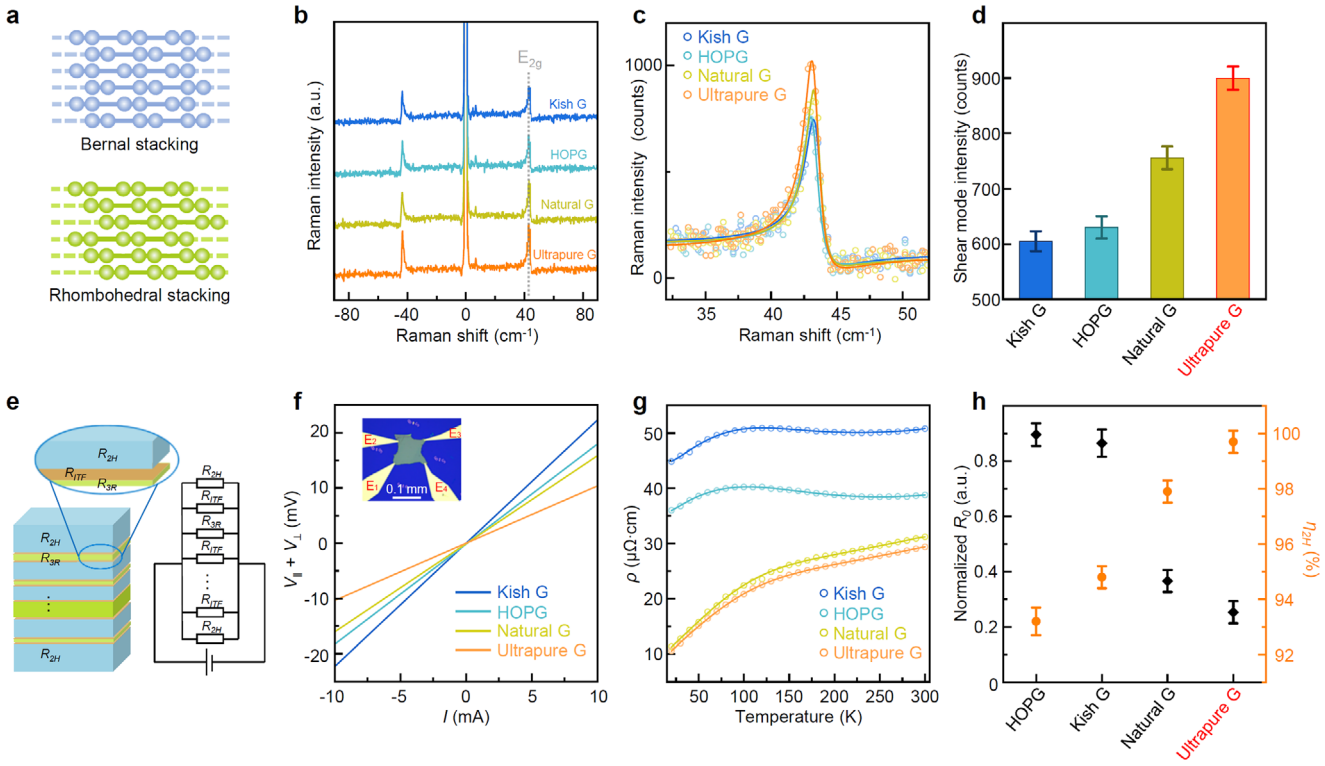

Figure 3. Out-of-plane structural purity characterization. a), The diagram of shear mode in Bernal stacked graphite and rhombohedral stacked graphite. b,c), The low-frequency Raman measurements of graphite samples (b) and their fitting curves of the E_{2g} peaks (c). d), The shear mode intensity of graphite samples extracted from the fitting parameters in (c). e), The diagram of the in-plane resistance, consisting of R_{2H}, R_{3R}, and R_{ITF}. f), The room-temperature *I*–*V* curves of graphite samples, insert: the optical image of the ultrapure graphite device. g), The in-plane resistivity of graphite samples as a function of temperature. h), The normalized interfacial residual resistance (R_0) and the ratio of Bernal phase (η_{2H}) of different graphite samples.

Based on the ultrahigh elemental, structural, and doping purities, the ultrapure graphite has great application potential of utilizing graphene devices to explore its intrinsic quantum physics.[31] By applying magnetic field on the standard Hall device, we obtained a well-resolved Landau fan diagram, which clearly indicated the evolution of the quantum Hall effect (QHE) with a magnetic field up to 9 T at the temperature of 1.7 K (Figure 4d). Considering the Dirac Hamiltonian with a fourfold symmetry of spin and valley, symmetry breaking at half filling (filling factor $\nu = 0$) and quarter filling ($\nu = 1$) were both clearly visible at fields of $B_{\perp} \gtrsim 4$ T (Figure 4e). Other high integer filling states were also visible at fields of $B_{\perp} \gtrsim 7$ T (Figure 4e; Figure S8a, Supporting Information). Moreover, the quantization of the $\nu = 2$ gap emerges at a very low magnetic field of only 0.3 T (Figure 4d and 4f). These fully developed symmetry breakings of spin and valley and ultralow quantum transition magnetic field in the graphene device are comparable with the best results from the previously reported QHE graphene devices,[32] demonstrating the extremely low defect density in our ultrapure graphite.

Further detailed Hall resistance (R_{xy}) and magnetoresistance (R_{xx}) at Landau levels of $\nu = 1$, 2, and 6 were detected, which is consistent with the theoretical quantum resistivity platforms in graphene devices[33] (Figure 4f). The mobility of our fabricated graphene device can also be calculated and reach a high value of ≈215 000 $cm^2\ V^{-1}\ s^{-1}$ (Figure S8b, Supporting Information), which is on par with the best results for exfoliated graphene with ultralow lattice disorders.[34] These distinct integer Landau levels and this high mobility demonstrate the superior potential of our as-grown graphite to observe abundant quantum physics.

3. Discussion

In conclusion, we propose a solid refining method with exceptional purification efficacy for eliminating extrinsic heteroatoms and reducing intrinsic defects in graphite. The obtained ultrapure graphite demonstrates ultrahigh elemental, structural, and doping purities, presenting extraordinary performance in quantum transport measurements. With a suitable metal choice, this successful solid refining process should be applicable to the purification of other layered vdW materials and even nonlayered conventional crystals and thus will allow for cutting-edge applications of ultrapure materials in the future.

4. Experimental Section

Solid Refining Process: Single-crystal Ni foils (99.994%, Zhongke Crystal Materials (Dongguan)) were placed on the surface of solid carbon sources (graphite paper, JL-AQC-5C, 99.9%, Beijing Jinglong Special Carbon Technology; activated carbon, R019801, Rhawn), and then were loaded together into a CVD furnace (Tianjin Kaiheng Co. Ltd., custom-designed). Then the furnace was heated to 1200–1300 °C for 2 h and the temperature was maintained for 10–30 h to grow graphite for one solid

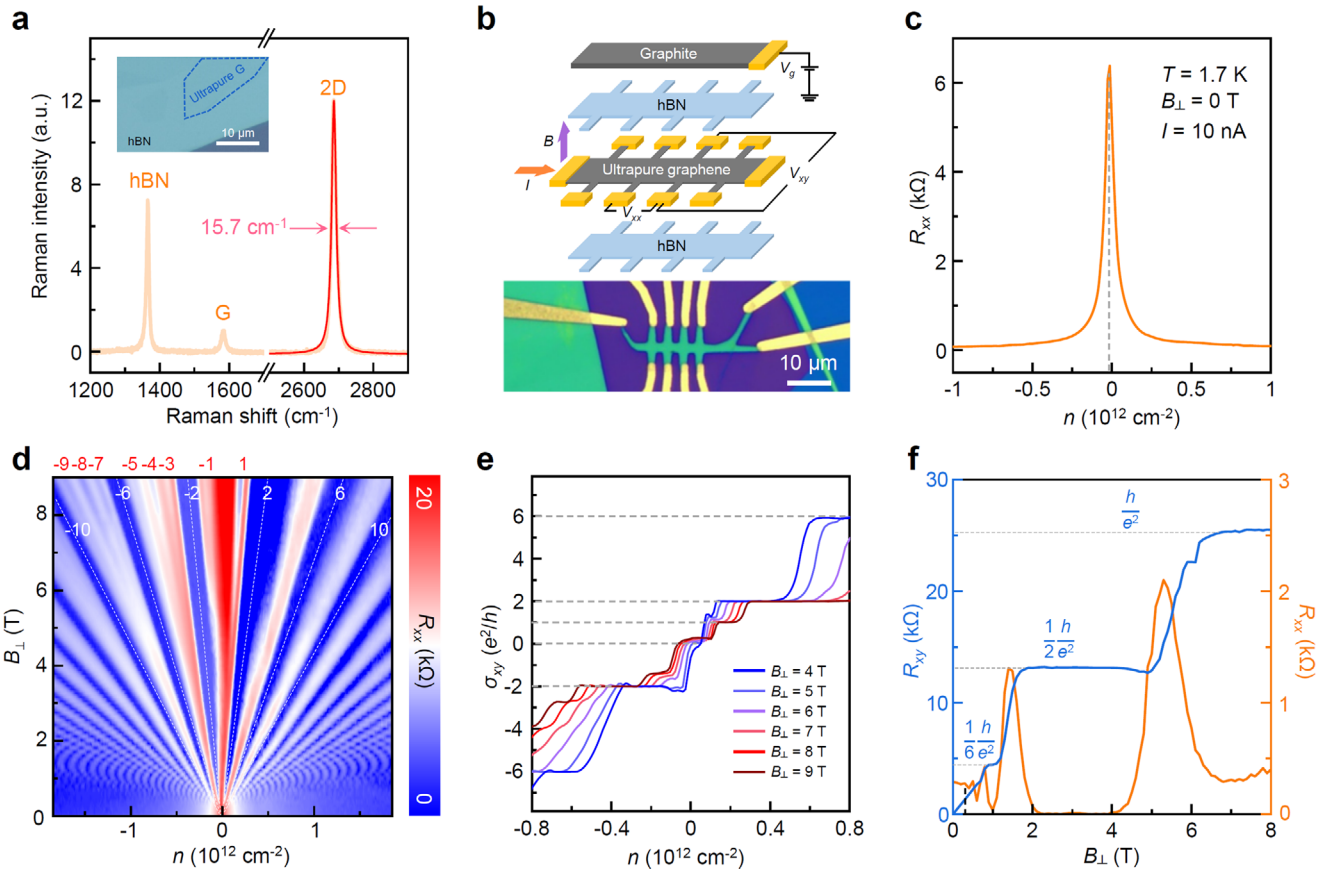

Figure 4. The doping purity characterization and quantum transport measurement. a), The Raman spectrum of the hBN/graphene/hBN heterostructure, insert: the optical image of the heterostructure. b), The diagram (top panel) and the optical image (bottom panel) of the QHE device. c), R_{xx} curve as a function of carrier density (n). d), The Landau fan diagram of R_{xx} of monolayer graphene as a function of both carrier density (n) and perpendicular magnetic field ($B_{\perp}$). All integer filling states are marked on the image. e), The Hall conductivity (σ_{xy}) curve as a function of n at $\nu = 0$ with different $B_{\perp}$. Symmetry breaking at half filling (filling factor $\nu = 0$) and quarter filling ($\nu = 1$) were both clearly visible at fields of $B_{\perp} \gtrsim 4$ T. Other high integer filling states were also visible at fields of $B_{\perp} \gtrsim 7$ T. f), R_{xy} and R_{xx} curves of graphene as a function of $B_{\perp}$ at $n = 1.4 \times 10^{11}$ cm^{-2}.

refining cycle. Throughout the growth experiments, 800 standard cubic centimeters per minute (sccm) Ar and 50 sccm H_2 flow through the tube furnace. H_2 was introduced to protect the Ni foil from oxidization. After that, another Ni foil was placed on the surface of the graphite for the next refining process.

Graphite Digestion Process for the ICP-MS Measurement: The sample was directly weighed in the quartz vessel, and a mixture of 0.75 mL of 14.4 mol L^{-1} HNO_3 and 0.25 mL of 12 mol L^{-1} HCl solvent was added. The vessel was placed in the micro-digester and heated at 260 °C for 1 h. After cooling, the resultant clear solution was transferred into the measuring flask (25 mL) and diluted to volume with water. Then the impurity elements were measured by ICP-MS.

Computational Details: The computational results presented in this work were carried out using the density functional theory as implemented in the Vienna Ab-initio Simulation Package.[35,36] The generalized gradient approximation (GGA) with the Perdew–Burke–Ernzerhof (PBE) exchange-correlation function was used with the plane-wave cut-off energy set at 400 eV for all calculations. The dispersion-corrected DFT-D_3 method was used because of its good description of long-range vdW interactions for 2D materials. The wave functions were expanded on plane-wave basis sets with the kinetic energy cutoff of 400 eV for all the systems studied. The geometries of the structures were relaxed until the force on each atom was less than 0.02 eV Å^{-1}, and the energy convergence criterion of 1×10^{-4} eV was met. A vacuum layer with a thickness of greater than 15 Å was used to avoid the interactions between two neighboring images.

To investigate the solid refining process of low-purity carbon sources, the structural properties and energetics for 13 kinds of common elements adsorbed in Ni bulk with a periodic stacking length of L = 10 were calculated. As for the Brillouin zone sampling, the Monkhorst-Pack grids of 3 × 3 × 1 was adopted. For comparing the diffusion barrier energy of Si/C/B atoms in Ni films, a model was constructed with a single Si/C/B atom adsorbed on six-layer Ni substrates with the bottom layer fixed, and 2 × 2 × 1 k-point meshes were adopted for these DFT calculations. The climbing-image nudged elastic band (NEB) method[37] was exploited to locate the diffusion energy barrier for the migration of extrinsic atoms in Ni.

Anisotropic H_2 Plasma Etching Process: The graphite samples were placed in the center of a quartz-tube furnace, and the radio frequency (13.56 MHz) coil was fixed at the entrance of the tube. After heating the sample to 500 °C with 40 sccm H_2 at a 50 Pa environment, a remote plasma with the power of 50 W was generated for 2 h to activate the H_2 into protons, etching the surface of the graphite sample. The H_2 etching was conducted exclusively for the AFM measurement to detect structural defects, and all other characterizations were carried out without plasma etching to accurately characterize the intrinsic properties of the graphite samples.

Shear Mode Measurement of Graphite: Low-frequency Raman spectra were measured at room temperature using a Jobin-Yvon HR800 micro-Raman system equipped with a charge-coupled detector (CCD) and a ×100 objective lens (numerical aperture = 0.9). The excitation wavelength was 633 nm from a He-Ne laser. A grating with 2400 lines per mm was used to

enable each CCD pixel to cover 0.19 cm^{-1} at 633 nm. Laser plasma lines were removed via a BragGrate bandpass filter (OptiGrate Corp.), and measurements down to 5 cm^{-1} were achieved using three BragGrate notch filters (OptiGrate Corp.). The laser power was kept below 1 mW to avoid sample heating.

A Breit-Wagner-Fano line shape was introduced to fit the interlayer E_{2g} modes of graphite (Figure 3c), which can be described as

$$I\ (\omega) = I_0\ \frac{[1 + 2\ (\omega - \omega_0)/(q\Gamma)]^2}{\left[1 + 4(\omega - \omega_0)^2/\Gamma^2\right]} \tag{1}$$

where I_0, ω_0, Γ, and $1/|q|$ are the intensity, uncoupled mode frequency, broadening parameter and coupling coefficient, respectively.

Exfoliation of Graphite and Graphene Samples: White tape (3 M Scotch) was used to exfoliate the synthesized graphite bulk as the mother tape. After several times of folding with another white tape, the graphite on tapes can be reduced into a very thin film. Then these tapes were pressed onto the SiO_2/Si substrate with enough contact and pulled slowly to leave few-layers and monolayer graphene samples on the substrate.

Device Fabrication and Van Der Pauw Electrical Measurement: The 100 nm thick graphite sample was exfoliated onto the SiO_2/Si substrate. A four-terminal mask was defined on the graphite surface by electron-beam lithography of a polymethyl methacrylate (PMMA) resist. Then metal leads were made (5 nm Cr/120 nm Au) by electron beam evaporation to ensure the contact.

The electrical resistance of the graphite sample can be divided into horizontal resistance ($R_{\parallel}$) and vertical resistance ($R_{\perp}$), which can be described as

$$R_{\parallel} = \frac{1}{2}\left(\frac{V_{12}}{I_{43}} + \frac{V_{34}}{I_{21}}\right) = \frac{V_{\parallel}}{I}, \quad R_{\perp} = \frac{1}{2}\left(\frac{V_{23}}{I_{14}} + \frac{V_{41}}{I_{32}}\right) = \frac{V_{\perp}}{I} \tag{2}$$

where $V_{\parallel}$ and $V_{\perp}$ represent the measured horizontal and vertical voltage. The electrical current I_{43}, I_{21}, I_{14}, and I_{32} were set to be the same value (I). Then the in-plane resistivity can be described as

$$\rho = \frac{\pi d}{\ln 2}\ \frac{R_{\parallel} + R_{\perp}}{2} f\left(\frac{R_{\parallel}}{R_{\perp}}\right) = \frac{\pi d}{\ln 2}\ \frac{V_{\parallel} + V_{\perp}}{2I} f\left(\frac{V_{\parallel}}{V_{\perp}}\right) \tag{3}$$

where f represents the van der Pauw correction factor.

Considering the resistivity of two stacking types ($R_{2H}(T)$ and $R_{3R}(T)$) and the interfacial resistance ($R_{ITF}(T)$) (Figure 3e), the total resistance ($R(T)$) of graphite can be described as

$$R\ (T)^{-1} = R_{2H}\ (T)^{-1} + R_{3R}(T)^{-1} + R_{ITF}(T)^{-1} \tag{4}$$

$$R_{2H}\ (T) = \alpha_{2H}\ T^{\frac{3}{2}} e^{\frac{E_{g1}}{2k_BT}},\ R_{3R}\ (T) = \alpha_{3R}\ T^{\frac{3}{2}} e^{\frac{E_{g2}}{2k_BT}},$$

$$R_{ITF}\ (T) = R_0 + R_1 T + R_2 e^{-\frac{E_a}{2k_BT}} \tag{5}$$

where the coefficients R_0, R_1, R_2, and the activation energy E_a in Equation (5) are free parameters. The temperature-independent term R_0 represents the residual resistance caused by the interfacial coupling. The parameters α_{2H}, α_{3R}, E_{g1}, and E_{g2} are weight ratio parameters and semiconducting energy gap for 2H and 3R phases, respectively. The weight ratio of 2H phase can be described as $\eta_{2H} = \frac{\alpha_{2H}}{\alpha_{2H}+\alpha_{3R}}$.

Applying Equation (4) to fit the temperature-dependent normalized resistivity, all these parameters can be extracted (Figure S7b; Table S2, Supporting Information).

Quantum Hall Device Fabrication and Transport Measurement: A modified dry transfer technique is carried out to fabricate the devices.[38] The polypropylene carbonate (PPC) film was used to pick up the hBN flake (exfoliated from hBN bulk crystals, from Shanghai Onway Technology), graphene (exfoliated from ultrapure graphite), and the hBN flake at 40 °C in sequence. Afterward, the sample was released on ultrapure graphite with SiO_2/Si substrate at 130 °C. Then a Hall-bar-shaped mask was defined on the top hBN surface by electron-beam lithography of a PMMA resist, and the top BN outside of the mask was etched by reactive ion etching (CHF_3:O_2 = 30:3) to expose the graphene edge. Finally, metal leads were deposited (5 nm Cr/80 nm Au) by electron beam evaporation to make electrical contact. After that, four-terminal transport measurements were performed using a lock-in amplifier at 17.777 Hz with a 10 nA current excitation in a 9 T superconducting magnet system at a temperature of 1.7 K.

Characterizations: Optical images were obtained using an Olympus BX51 microscope. AFM images were acquired using an Asylum Research Cypher system. ICP-MS was measured using a NexION 350X system. EBSD characterizations were carried out using a PHI 710 scanning Auger nanoprobe instrument. Raman spectra were measured at room temperature using a Jobin-Yvon HR800 micro-Raman system equipped with a CCD and a ×100 objective lens (numerical aperture = 0.9). The excitation wavelength is 532 nm from a diode-pumped solid-state laser. A grating with 2400 lines per mm was used to enable each CCD pixel to cover 0.29 cm^{-1} at 532 nm. The laser power was kept below 1 mW to avoid sample heating. STEM experiments were performed in FEI Titan Themis G2 300 operated at 300 kV. HR-XRD 2θ scan measurements were conducted using a Bruker D8 Discover system with a Cu Kα_1 X-ray source.

Supporting Information

Supporting Information is available from the Wiley Online Library or from the author.

Acknowledgements

M.D., Z. Zhang, and W.W. contributed equally to this work. This work was supported by the National Key R&D Program of China (2023YFB4603603, 2022YFA1403500, 2024YFA1208201, 2021YFA1400204, and 2021YFA1400502), the National Natural Science Foundation of China (52025023, 52402043, 12334001, 52427802, 52021006, 12404209, T242200539, and 52272173), the Guangdong Major Project of Basic and Applied Basic Research (2021B0301030002). This work has been supported by the New Cornerstone Science Foundation through the XPLORER PRIZE to K.L.

Conflict of Interest

The authors declare no conflict of interest.

Author Contributions

X.B. and K.L. supervised the project. K.L. conceived the experiments. M.D. and Z. Zhang conducted the growth experiments and ICP-MS measurements. M.D., Z. Zhou, L.W., and X.X. performed the H_2 etching and AFM measurements. M.D., H.W., X.C., and P.T. performed the low-frequency Raman measurements. M.D., X.B., Q.G., M.Z., Y.F., Q.Y., and M.W. performed the TEM and EBSD experiments. M.D., J.D., W.Y., and G.Z. performed the electronic transport experiments. W.W. and F.D. carried out the theoretical calculations. M.D., Z. Zhang, W.W., and K.L. wrote the article. X.B., G.Z., P.T., and E.W. revised the manuscript. All the authors discussed the results and commented on the manuscript.

Data Availability Statement

The data that support the findings of this study are available from the corresponding author upon reasonable request.

Keywords

graphene, solid refining, Ultrapure graphite

Received: January 7, 2025
Revised: April 23, 2025
Published online: May 6, 2025

[1] A. S. Myerson, *Handbook of Industrial Crystallization*, Butterworth-Heinemann, Boston **2002**.
[2] J. Czochralski, *Z. Anorg. Phys. Chem.* **1918**, *92*, 219.
[3] P. W. Bridgman, *Proc. Am. Acad. Arts Sci.* **1925**, *60*, 305.
[4] D. C. Stockbarger, *Rev. Sci. Instrum.* **1936**, *7*, 133.
[5] S. Kyropoulos, *Z. Anorg. Allg. Chem.* **1926**, *154*, 308.
[6] Y. Cao, V. Fatemi, S. Fang, K. Watanabe, T. Taniguchi, E. Kaxiras, P. Jarillo-Herrero, *Nature* **2018**, *556*, 43.
[7] M. Yankowitz, S. W. Chen, H. Polshyn, Y. X. Zhang, K. Watanabe, T. Taniguchi, D. Graf, A. F. Young, C. R. Dean, *Science* **2019**, *363*, 1059.
[8] H. Zhou, T. Xie, A. Ghazaryan, T. Holder, J. R. Ehrets, E. M. Spanton, T. Taniguchi, K. Watanabe, E. Berg, M. Serbyn, A. F. Young, *Nature* **2021**, *598*, 429.
[9] Z. Lu, T. Han, Y. Yao, A. P. Reddy, J. Yang, J. Seo, K. Watanabe, T. Taniguchi, L. Fu, L. Ju, *Nature* **2024**, *626*, 759.
[10] H. Park, J. Q. Cai, E. Anderson, Y. N. Zhang, J. Y. Zhu, X. Y. Liu, C. Wang, W. Holtzmann, C. W. Hu, Z. Y. Liu, T. Taniguchi, K. Watanabe, J. H. Chu, T. Cao, L. Fu, W. Yao, C. Z. Chang, D. Cobden, D. Xiao, X. D. Xu, *Nature* **2023**, *622*, 74.
[11] Y. Machida, N. Matsumoto, T. Isono, K. Behnia, *Science* **2020**, *367*, 309.
[12] J. Billaud, F. Bouville, T. Magrini, C. Villevieille, A. R. Studart, *Nat. Energy* **2016**, *1*, 16097.
[13] S. Ghosh, W. Z. Bao, D. L. Nika, S. Subrina, E. P. Pokatilov, C. N. Lau, A. A. Balandin, *Nat. Mater.* **2010**, *9*, 555.
[14] Q. Zhou, J. L. Zheng, S. Onishi, M. F. Crommie, A. K. Zettl, *Proc. Natl. Acad. Sci.* **2015**, *112*, 8942.
[15] M. F. El-Kady, V. Strong, S. Dubin, R. B. Kaner, *Science* **2012**, *335*, 1326.
[16] A. R. Tron, The production and uses of natural graphite, Her Majesty's Stationery Office, London **1964**.
[17] S. L. Liu, C. R. Loper, *Carbon* **1991**, *29*, 547.
[18] L. C. F. Blackman, A. R. Ubbelohde, *Proc. Roy. Soc. A* **1962**, *226*, 20.
[19] W. G. Pfann, *Zone melting*, John Wiley & Sons, Oxford, England **1966**.
[20] Z. Zhang, M. Ding, T. Cheng, R. Qiao, M. Zhao, M. Luo, E. Wang, Y. Sun, S. Zhang, X. Li, Z. Zhang, H. Mao, F. Liu, Y. Fu, K. Liu, D. Zou, C. Liu, M. Wu, C. Fan, Q. Zhu, X. Wang, P. Gao, Q. Li, K. Liu, Y. Zhang, X. Bai, D. Yu, F. Ding, E. Wang, K. Liu, *Nat. Nanotechnol.* **2022**, *17*, 1258.
[21] T. B. Massalski, H. Okamoto, P. R. Subramanian, L. Kacprzak, *Binary Alloy Phase Diagrams*, ASM International, OH, USA **1990**.
[22] R. Yang, L. C. Zhang, Y. Wang, Z. W. Shi, D. X. Shi, H. J. Gao, E. G. Wang, G. Y. Zhang, *Adv. Mater.* **2010**, *22*, 4014.
[23] X. Zhang, W.-P. Han, X.-F. Qiao, Q.-H. Tan, Y.-F. Wang, J. Zhang, P.-H. Tan, *Carbon* **2016**, *99*, 118.
[24] P. H. Tan, W. P. Han, W. J. Zhao, Z. H. Wu, K. Chang, H. Wang, Y. F. Wang, N. Bonini, N. Marzari, N. Pugno, G. Savini, A. Lombardo, A. C. Ferrari, *Nat. Mater.* **2012**, *11*, 294.
[25] Y. W. Tan, Y. Zhang, K. Bolotin, Y. Zhao, S. Adam, E. H. Hwang, S. D. Sarma, H. L. Stormer, P. Kim, *Phys. Rev. Lett.* **2007**, *99*, 246803.
[26] L. Lin, J. C. Zhang, H. S. Su, J. Y. Li, L. Z. Sun, Z. H. Wang, F. Xu, C. Liu, S. Lopatin, Y. H. Zhu, K. C. Jia, S. L. Chen, D. R. Rui, J. Y. Sun, R. W. Xue, P. Gao, N. Kang, Y. Han, H. Q. Xu, Y. Cao, K. S. Novoselov, Z. Q. Tian, B. Ren, H. L. Peng, Z. F. Liu, *Nat. Commun.* **2019**, *10*, 1912.
[27] L. Banszerus, M. Schmitz, S. Engels, J. Dauber, M. Oellers, F. Haupt, K. Watanabe, T. Taniguchi, B. Beschoten, C. Stampfer, *Sci. Adv.* **2015**, *1*, 1500222.
[28] J. Amontree, X. Yan, C. S. DiMarco, P. L. Levesque, T. Adel, J. Pack, M. Holbrook, C. Cupo, Z. Wang, D. Sun, A. J. Biacchi, C. E. Wilson-Stokes, K. Watanabe, T. Taniguchi, C. R. Dean, A. R. Hight Walker, K. Barmak, R. Martel, J. Hone, *Nature* **2024**, *630*, 636.
[29] G. W. Yuan, W. L. Liu, X. L. Huang, Z. H. Wan, C. Wang, B. Yao, W. J. Sun, H. Zheng, K. H. Yang, Z. J. Zhou, Y. F. Nie, J. Xu, L. B. Gao, *Nat. Commun.* **2023**, *14*, 5457.
[30] M. Wang, M. Huang, D. Luo, Y. Li, M. Choe, W. K. Seong, M. Kim, S. Jin, M. Wang, S. Chatterjee, Y. Kwon, Z. Lee, R. S. Ruoff, *Nature* **2021**, *596*, 519.
[31] W. Zhu, D. N. Sheng, *Phys. Rev. Lett.* **2019**, *123*, 056804.
[32] A. F. Young, C. R. Dean, L. Wang, H. Ren, P. Cadden-Zimansky, K. Watanabe, T. Taniguchi, J. Hone, K. L. Shepard, P. Kim, *Nat. Phys.* **2012**, *8*, 550.
[33] Y. Zhang, Z. Jiang, J. P. Small, M. S. Purewal, Y. W. Tan, M. Fazlollahi, J. D. Chudow, J. A. Jaszczak, H. L. Stormer, P. Kim, *Phys. Rev. Lett.* **2006**, *96*, 136806.
[34] A. M. Seiler, F. R. Geisenhof, F. Winterer, K. Watanabe, T. Taniguchi, T. Y. Xu, F. Zhang, R. T. Weitz, *Nature* **2022**, *608*, 298.
[35] G. Kresse, J. Hafner, *Phys. Rev. B* **1993**, *48*, 13115.
[36] G. Kresse, J. Furthmuller, *Comp. Mater. Sci.* **1996**, *6*, 15.
[37] G. Mills, H. Jonsson, G. K. Schenter, *Surf. Sci.* **1995**, *324*, 305.
[38] F. Pizzocchero, L. Gammelgaard, B. S. Jessen, J. M. Caridad, L. Wang, J. Hone, P. Bøggild, T. J. Booth, *Nat. Commun.* **2016**, *7*, 11894.

Supporting Information

Ultrapure graphite from solid refining

Mingchao Ding[#], Zhibin Zhang[#], Wenya Wei[#], Heng Wu, Xue Chen, Jingwei Dong, Quanlin Guo, Mengze Zhao, Ziqi Zhou, Li Wang, Xiaozhi Xu, Ying Fu, Wei Yang, Muhong Wu, Quanzhan Yang, Feng Ding, Enge Wang, Pingheng Tan*, Guangyu Zhang*, Kaihui Liu*, and Xuedong Bai*

The supporting information includes:

Figure S1-S8

Table S1 and S2

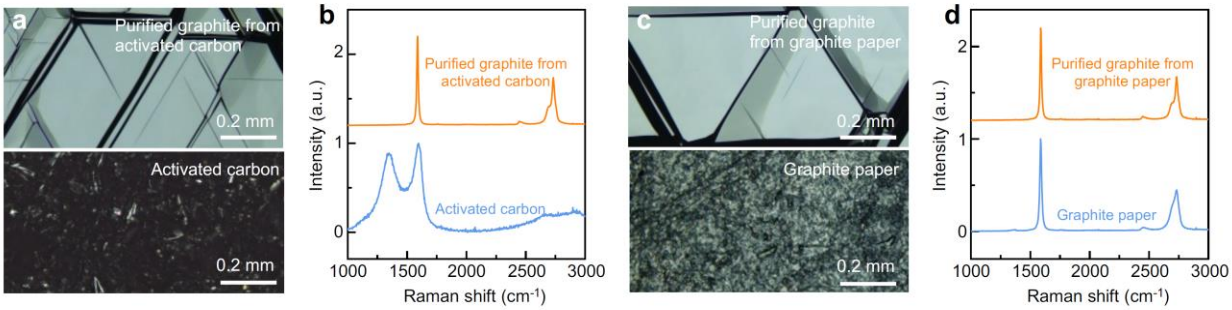

Figure S1 | Graphite purified from different carbon sources. a-b), The optical images (a) and Raman spectra (b) of activated carbon (bottom panel) and the purified graphite from activated carbon (top panel). **c-d),** The optical images (c) and Raman spectra (d) of graphite paper (bottom panel) and the purified graphite from graphite paper (top panel).

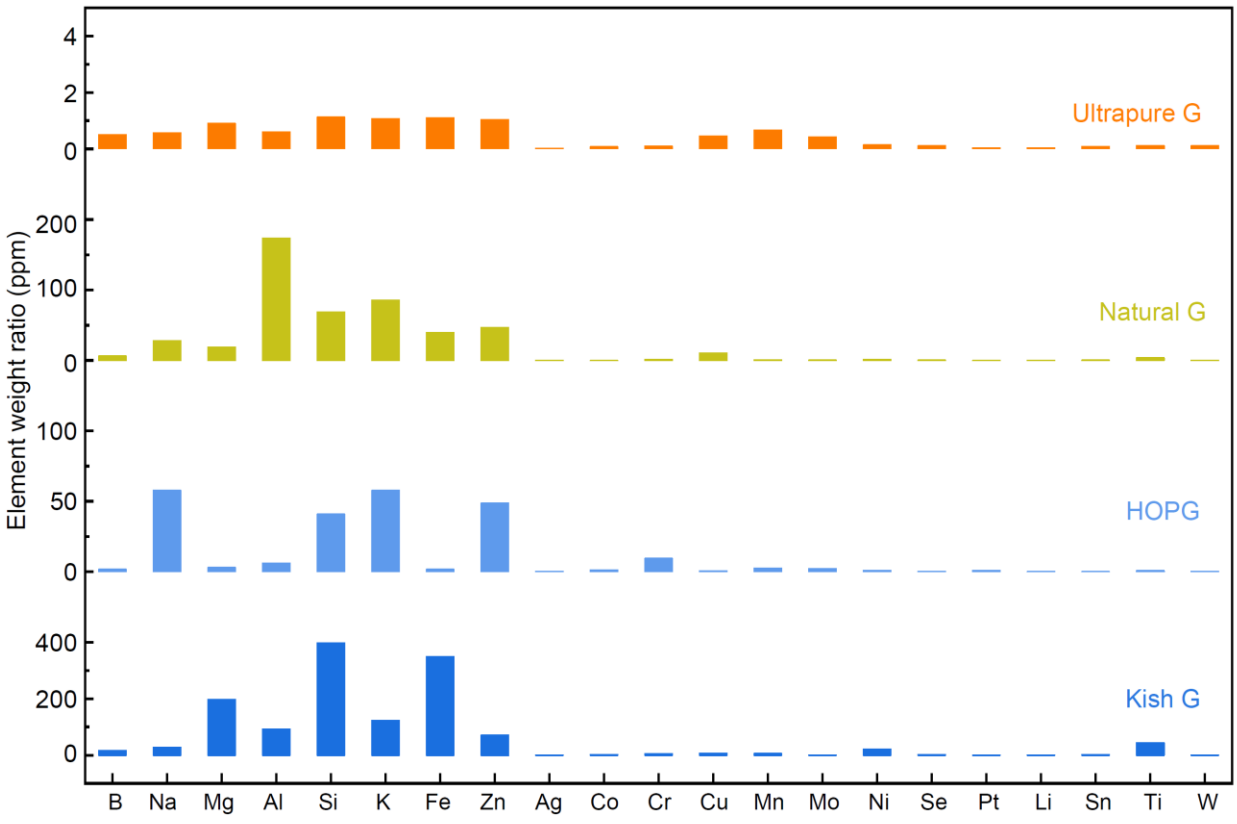

Figure S2 | Elemental purity characterization of different graphite samples.

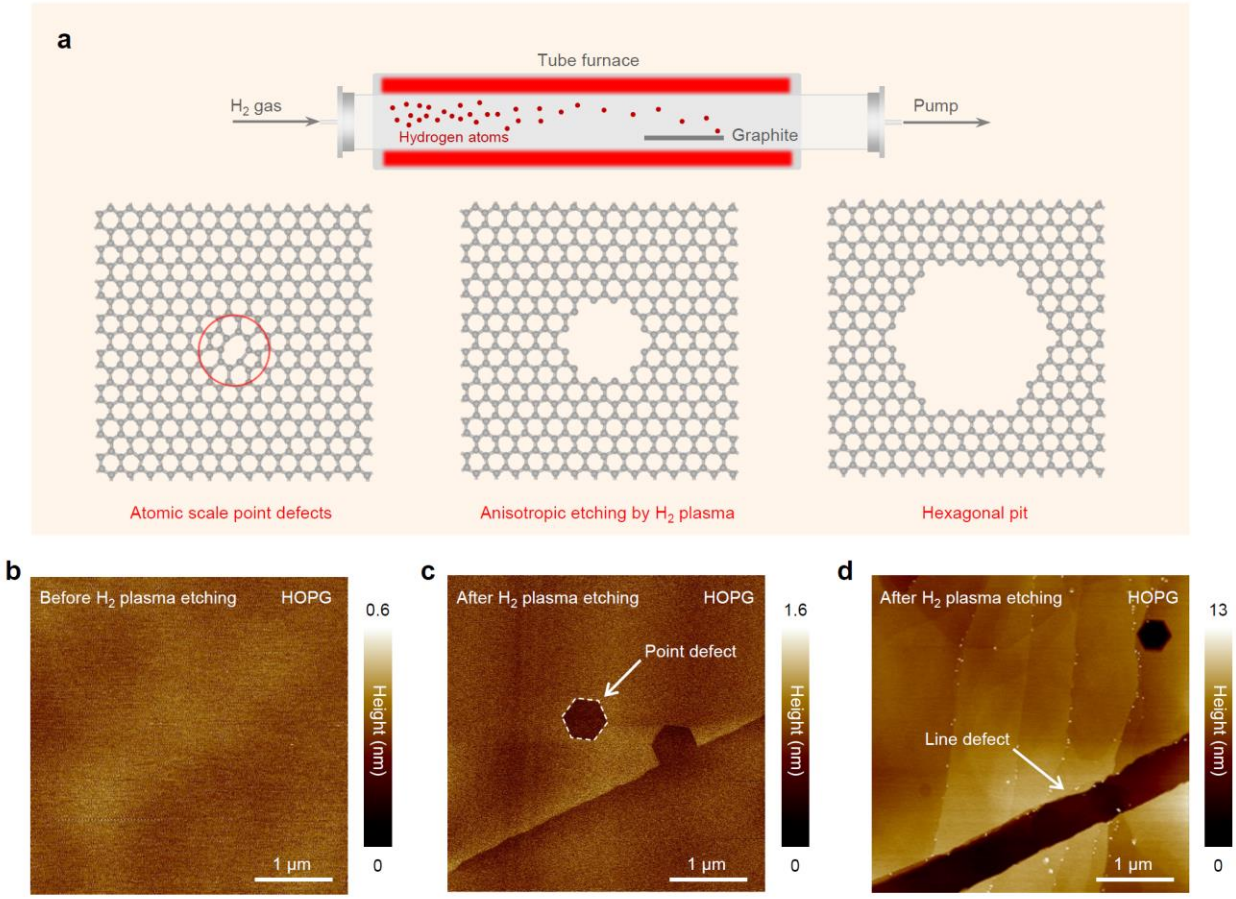

Figure S3 | Characterization of point and line defects of graphite. a), The diagram of H_2 plasma etching process on the defects of graphite. The H_2 plasma will etch the atomic scale defect sites into hexagonal pits with zigzag edges. **b),** The AFM image of HOPG before the H_2 etching process. **c-d),** The AFM images of point defect (c) and line defect (d) on HOPG after being etched by H_2 plasma.

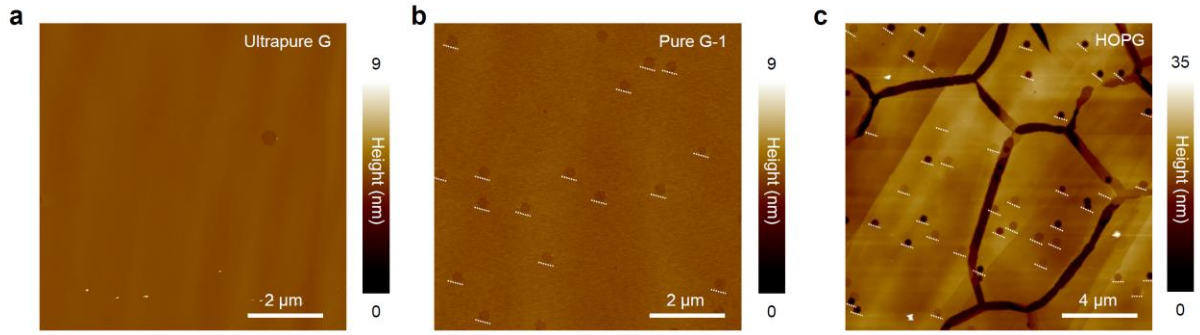

Figure S4 | Crystallinity characterization of different graphite samples. a-c), The AFM images of ultrapure graphite (a), pure G-1 (b), and HOPG (c) after the H_2 plasma etching process. The orientations of the hexagonal pits in pure G-1 are highly aligned, while those in distinct HOPG domains are different and the boundaries between domains are clearly observed.

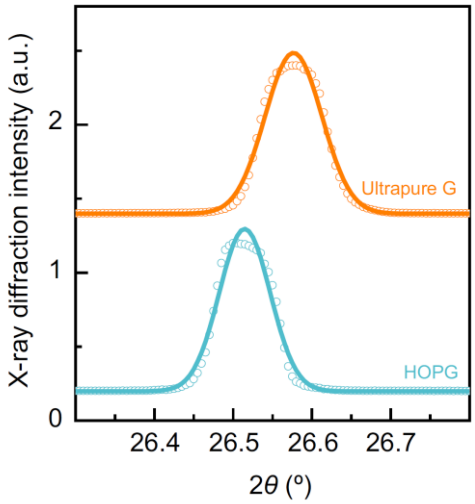

Figure S5 | HR-XRD 2θ-scan results of ultrapure graphite (top panel) and HOPG (bottom panel). The (0002) peak of ultrapure graphite sample is observed at a 2θ angle of 26.58°, corresponding to a calculated interlayer spacing of ~0.335 nm (top panel). The (0002) peak of HOPG appears at a slightly lower 2θ angle of 26.51°, corresponding to a larger interlayer spacing of ~0.336 nm (bottom panel).

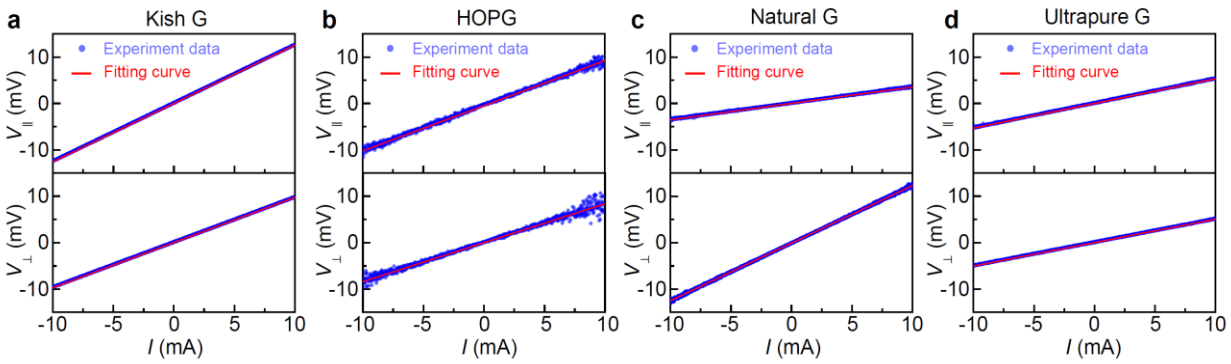

Figure S6 | The in-plane electrical conductivity measurements of different graphite samples at room temperature.

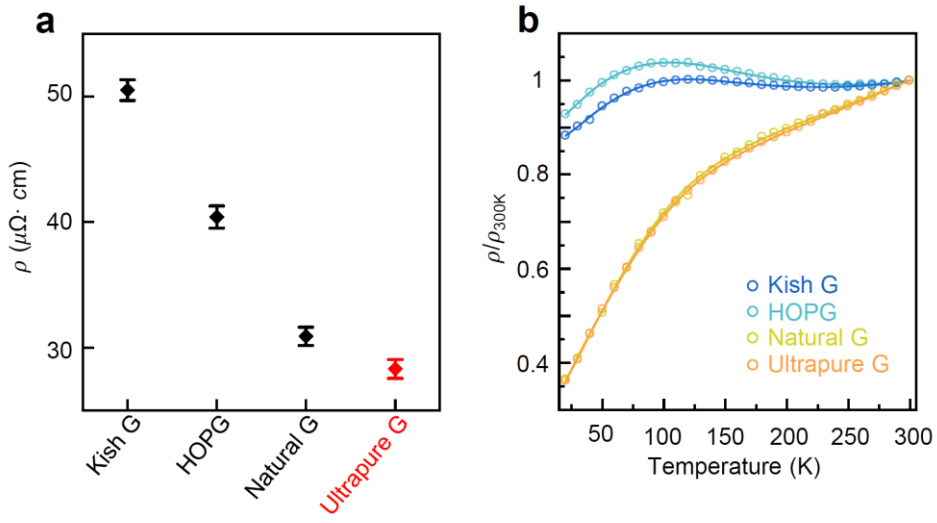

Figure S7 | The in-plane electrical conductivity measurements. a), The in-plane electrical resistivity of different graphite samples at room temperature. **b),** The normalized temperature-dependent in-plane electrical resistivity of different graphite samples.

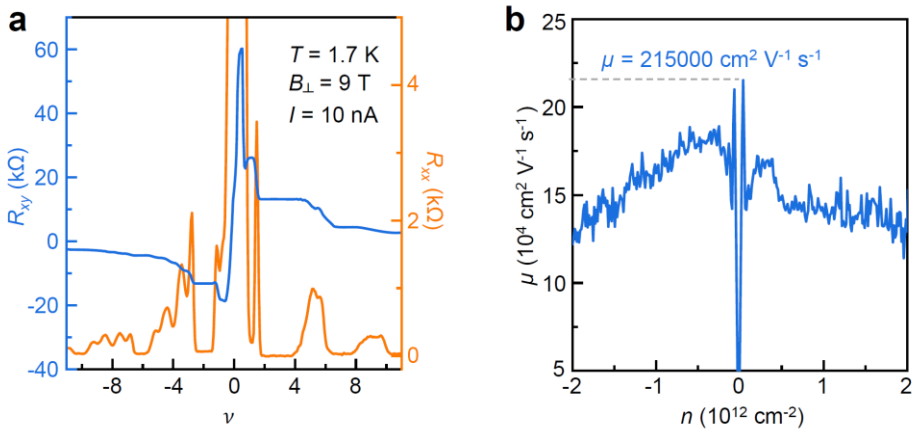

Figure S8 | Electronic transport measurements of the Hall device. a),The R_{xx} and R_{xy} curves as a function of ν when $B_{\perp}$ = 9 T. All integer Landau levels are visible. **b),** The mobility (μ) as a function of n.

Table S1 | Purity comparison of different kinds of graphite.

Purity	Kish graphite	HOPG	Natural graphite	Ultrapure graphite
Elemental defect density	1480 ppm	200 ppm	480 ppm	10 ppm
In-plane structural defect density	38.9 ppb	17.1 ppb	11.8 ppb	0.2 ppb
Out-of-plane stacking purity	94.8%	93.2%	97.9%	99.7%

Table S2 | The resistance fitting parameters of different graphite samples.

Resistance fitting parameter	Kish graphite	HOPG	Natural graphite	Ultrapure graphite
R_0	0.86	0.89	0.26	0.25
R_1	6.50×10^{-4}	1.33×10^{-3}	4.89×10^{-3}	4.11×10^{-3}
R_2	0.31	0.16	0.01	0.10
E_a (meV)	15	12	4	5
α_{2H}	2.54×10^{-3}	1.27×10^{-3}	3.40×10^{-3}	3.11×10^{-2}
α_{3R}	1.40×10^{-4}	9.25×10^{-5}	7.42×10^{-5}	7.94×10^{-5}
E_{g1} (meV)	40	50	47	43
E_{g2} (meV)	101	112	97	99